Particle stresses in dilute, polydisperse, two-way coupled turbulent flows

David H. Richter, Omar Garcia, and Christopher Astephen
Department of Civil and Environmental Engineering and Earth Sciences, University of Notre Dame, Notre Dame, Indiana 46556, USA
(Received 24 June 2015; revised manuscript received 4 September 2015; published 11 January 2016)

Direct numerical simulations are performed of turbulent planar Couette flow which are seeded with two-way coupled particles at low volume concentration. Based on an understanding of the development of particle stress (horizontal momentum carried vertically on average by the particle phase) in monodisperse systems at various particle Stokes numbers, several bidisperse and continuously polydisperse systems are simulated which are chosen to understand how flows containing blends of particle Stokes numbers can be effectively modeled in the dilute regime. Under noninteracting conditions, the particle stresses from particles with different inertia and different feedback stresses are shown to be linearly additive, providing a convenient method for effectively representing dispersed phase stress in polydisperse systems. While this is true, it is demonstrated that a single effective particle size is in general not sufficient at representing the entire mixture.

DOI: 10.1103/PhysRevE.93.013111

I. INTRODUCTION

In the limit of high density ratio and low volume concentration, the Lagrangian point particle method two-way coupled to a turbulent flow computed via direct numerical simulation (DNS) has been used extensively to probe the phenomena of turbulence modification by a dispersed phase [1]. Specifically, in wall-bounded flows, these small, heavy particles are seen to collect near the walls through the process of turbophoresis [2], while at the same time experiencing preferential concentration which is maximized at a Stokes number near unity [3]. Both of these processes result in varying degrees of effectiveness of particle-induced modulation of the carrier phase flow as a function of particle inertia. In nearly all previous studies of two-way coupled wall-bounded flow, however, the dispersed phase is assumed to be monodisperse. Even in studies which consider evaporating droplets [4], the droplet size distributions remain relatively narrow.

This study aims to extend previous simulations of planar Couette flow [5–7] by considering the two-way coupling in polydisperse systems. We focus entirely on the dilute limit, in that particle-particle interactions are not considered, and thus any couplings between particle sizes will be indirect—i.e., coupling to the carrier phase flow of one particle type may enhance or inhibit the two-way coupling of other types. While the effects of particle collisions in polydisperse systems can be quite important [8], effectively modeling the particle stress of polydisperse systems is relevant in many environments where volume concentrations remain quite low, such as windborne spray or dust at heights $O(1\ m)$ above the surface.

Richter and Sullivan [5] showed that reductions of the carrier phase Reynolds stress are maximized when the Stokes number based on the centerline Kolmogorov scale St_K is order unity, and that particles with $\mathrm{St}_K = O(1)$ could reduce turbulent vortical motions near the wall twice as efficiently as particles with $\mathrm{St}_K = O(10)$. At low Reynolds numbers, this Stokes-number-dependent reduction in the Reynolds stress was shown to be nearly exactly offset by the dispersed phase stress, in such a way that the total stress remains nearly constant across various particle types. Richter and Sullivan [6] then illustrated that $\mathrm{St}_K = O(1)$ particles preferentially concentrate in exactly the regions associated with the Reynolds-stress-producing ejection motions at the wall, hence their efficient reduction of the turbulent stress, while particles with higher Stokes numbers of $\mathrm{St}_K = O(10)$ and $\mathrm{St}_K = O(100)$ are not able to collect in these regions and thus their reduction of the Reynolds stress (and the resulting increase of the particle stress) remains smaller in magnitude.

After further establishing and characterizing the particle stress which develops in monodisperse systems, the present simulations first consider bidisperse systems, with the goal of determining the overall degree of two-way coupling when particles with different clustering characteristics are together in the same flow. Once it is shown that the particle stresses for these bidisperse systems are nearly additive, polydisperse systems are considered which contain equal mass contributions in the Stokes number range 1–100.

II. NUMERICAL SETUP

Details of the numerical method are contained elsewhere [5–7], and only a brief summary will be provided herein. DNS is performed on the carrier phase using a pseudospectral discretization in the periodic, homogeneous x and y directions and second-order finite differences in the wall-normal z direction. Time integration is performed via a third order Runge-Kutta scheme. The carrier phase is assumed incompressible, and thus the equations governing mass and momentum conservation are given by

$$\frac{\partial u_j}{\partial x_j} = 0, \tag{1}$$

and

$$\frac{\partial u_i}{\partial t} + u_j \frac{\partial u_i}{\partial x_j} = -\frac{1}{\rho_f}\frac{\partial p}{\partial x_i} + \nu_f \frac{\partial^2 u_i}{\partial x_j^2} + \frac{1}{\rho_f} F_{p,i}, \tag{2}$$

where u_i is the carrier phase velocity, ρ_f is the carrier phase density, and ν_f is the carrier phase kinematic viscosity. $F_{p,i}$ is the coupling force due to the dispersed phase, which is computed at a node by summing the individual projected particle drag forces which occur within a grid cell length in all three directions.

Gravity is neglected, and the dispersed phase is assumed to have a density much larger than the carrier phase density.

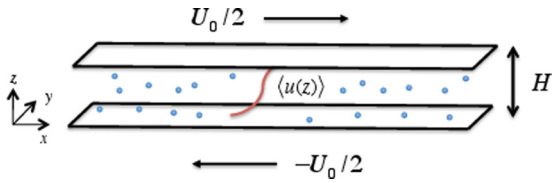

FIG. 1. Simulation domain schematic. Plate velocity difference is U_0 and plate separation is H. Example mean velocity profile shown in red.

Thus the only force considered is the drag force [9], which is assumed to be the Stokes drag with an empirical Reynolds number correction [10]:

$$v_{p,i} = \frac{dx_{p,i}}{dt}, \tag{3}$$

$$\frac{dv_{p,i}}{dt} = \frac{\left(1 + 0.15\mathrm{Re}_p^{0.687}\right)}{\tau_p}(u_{f,i} - v_{p,i}), \tag{4}$$

where $u_{f,i}$ is the carrier phase velocity interpolated to the particle location using sixth order Lagrange interpolation, $\tau_p = \rho_p d_p^2/18\rho_a \nu_a$ is the Stokes acceleration time scale of the particle, and $\mathrm{Re}_p = d_p|u_{f,i} - v_{p,i}|/\nu_f$ is the particle Reynolds number. The particle diameter and density are given by d_p and ρ_p, respectively.

Turbulent planar Couette flow develops between two plates moving with equal and opposite velocities, where U_0 is the velocity difference and H is the distance between the walls—see Fig. 1. A grid of $[N_x, N_y, N_z] = [128, 256, 128]$ on a domain size of $[L_x, L_y, L_z] = [2\pi H, 2\pi H, H]$ is used for the carrier phase calculations. The bulk Reynolds number of the flow, defined as $\mathrm{Re}_b = U_0 H/\nu_f$, is set to 8000, which leads to a friction Reynolds number of $\mathrm{Re}_\tau \approx 120$, where $\mathrm{Re}_\tau = u_\tau H/2\nu_f$ is based on the standard friction velocity u_τ. Both the streamwise and spanwise domain distances are too small to avoid artificial confinement of the large-scale Couette structures which form in this flow, but for the purposes of this study this effect does not preclude a study of the effects of polydispersity on particle stresses. Furthermore turbulent statistics such as the Reynolds stress are relatively insensitive to this confinement [11]. Turbulent Couette flow is chosen because (a) the total stress is uniform with height and (b) the presence of the large structures provides an additional time and length scale with which the particles can interact in addition to the "typical" near-wall streaks and vortices found in turbulent channel flow.

Boundary conditions for the carrier phase are no-slip at both walls and periodic in the horizontal directions. Particles bounce elastically from the walls at a distance of one viscous unit (as opposed to their radius—see discussion in Richter and Sullivan [5]). Averages are performed for nondimensional times of at least $tU_0/H = 5000$ after a statistically steady state has been developed, except in noted cases where slow turbophoretic processes prevent a statistical stationary state to develop in a reasonable amount of time.

The particle Stokes number, $\mathrm{St}_K = \tau_p/\tau_K$ is defined based on the acceleration time scale τ_p and the Kolmogorov time scale computed directly from the dissipation rate at the channel centerline. In many other studies, the Stokes number is instead defined based on viscous wall units rather than τ_K, but we choose the current definition since $\mathrm{St}_K \approx 1$ corresponds to the peak in the reduction of the carrier phase Reynolds stress. Regarding the time discretization, a Courant-Friedrichs-Lewy (CFL) parameter of 0.6 ensures that the ratio of $\tau_p/\Delta t$, where Δt is the simulation time step, remains larger than 5 for all Stokes numbers.

Three sets of simulations are performed: (1) a series of monodisperse simulations to determine the distinct Stokes number regimes which exist in the two-way coupled system, (2) a set of bidisperse simulations where binary mixtures of particles from the set $\mathrm{St}_K \approx [1, 10, 100]$ are used to understand simple combinations of particles from each of the distinct Stokes number regimes, and (3) a series of polydisperse simulations where power-law-distributed blends of particles for various ranges within $1 < \mathrm{St}_K < 100$ are used to develop a low-order method for representing the mixture. In all simulations the mass fraction is fixed at a value of $\phi_m = 0.25$.

III. RESULTS

A. Monodisperse simulations

Before discussing the effects of polydispersity, we first summarize the behavior of two-way coupled monodisperse simulations, focusing particularly on particle-induced modifications to momentum fluxes across the domain. Figure 2 shows the total upwards (positive z) momentum flux τ_{tot}, broken up into its turbulent $\tau_{\mathrm{turb}} = \rho_f \langle u'w' \rangle$, viscous $\tau_{\mathrm{vis}} = -\rho_f \nu_f \frac{d\langle u \rangle}{dz}$, and particle-induced $\tau_{\mathrm{part}} = \langle C \rangle \langle u'_p w'_p \rangle_c$ components, where $C(z)$ is the mass concentration, u'_p and w'_p are the fluctuating particle velocities, and $\langle \cdot \rangle_c$ refers to a mass-weighted average over the particle phase in a horizontal slab of height Δz (see Richter and Sullivan [5] for a more detailed description of this

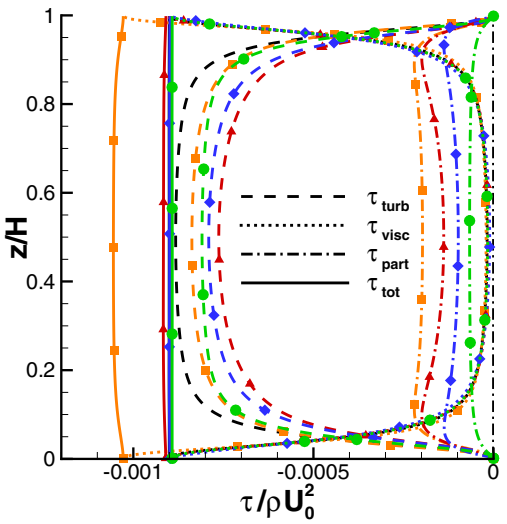

FIG. 2. Stress components for $\mathrm{St}_K \approx 0.1$ (orange, squares), $\mathrm{St}_K \approx 1.0$ (red, triangles), $\mathrm{St}_K \approx 10$ (blue, diamonds), $\mathrm{St}_K \approx 100$ (green, circles), and unladen (black, no symbol) as a function of z/H. Line types: solid corresponds to total stress τ_{tot}, dashed to turbulent stress τ_{turb}, dotted to viscous stress τ_{visc}, and dash-dotted to particle stress τ_{part}.

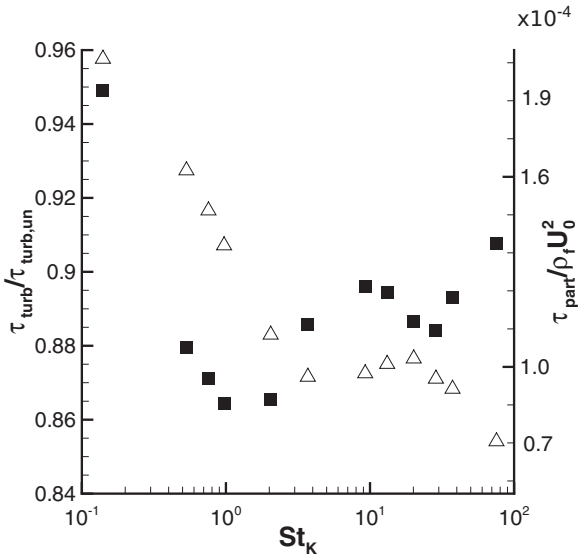

FIG. 3. Solid squares (left axis): turbulent stress $\tau_{\text{turb}} = \rho_f \langle u'w' \rangle$ evaluated at the centerline, normalized by the unladen value at the centerline $\tau_{\text{turb,un}}$ plotted as a function of St_K. Hollow triangles (right axis): normalized particle stress $\tau_{\text{part}}/\rho_f U_0^2$ as a function of St_K.

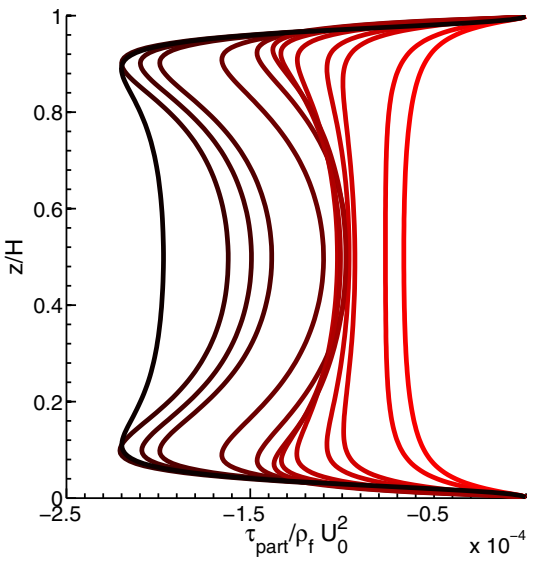

FIG. 4. Normalized particle stress $\tau_{\text{part}}/\rho_f U_0^2$ as a function of z/H. Shown are profiles for Stokes numbers corresponding to each point in Fig. 3. The Stokes number increases from $\text{St}_K \approx 0.1$ to $\text{St}_K \approx 100$ as the color transitions from black to red (from left towards right; dark to light shade).

breakdown). Contained in Fig. 2 is the unladen case and laden cases at $\text{St}_K \approx [0.1, 1.0, 10, 100]$.

Figure 2 shows that the total stress (solid lines) remains nearly unchanged for all St_K, except when $\text{St}_K \approx 0.1$. In this case, the particles have very little inertia and nearly act as fluid tracers. In the limit of $\text{St}_K \to 0$ while maintaining a constant mass fraction, the particles effectively increase the density of the carrier phase (see for example Lee and Lee [12]), and in this case the total stress would be increased by 25%. For $\text{St}_K \approx 0.1$, it is this behavior which results in a total stress magnitude which exceeds that for all other cases. Also note for $\text{St}_K \approx 0.1$ that the total stress slightly deviates from a uniform vertical profile; this is due to the slow turbophoretic processes at this low Stokes number and corresponding lack of statistical stationarity.

For $\text{St}_K \geqslant 1$, on the other hand, reductions in the turbulent stress (dashed lines) are nearly exactly compensated by a rise in the particle stress (dash-dotted lines), and it is these cases in which we are primarily interested since the particles possess appreciable inertia, as measured by St_K. Figure 2 suggests that the maximum reduction of the turbulent stress occurs when $\text{St}_K = O(1)$, with a peak of the particle stress among $\text{St}_K \geqslant 1$.

To confirm this behavior Fig. 3 plots two quantities: (1) the ratio $\tau_{\text{turb}}/\tau_{\text{turb,un}}$, where $\tau_{\text{turb,un}}$ is the turbulent stress for the unladen case and (2) the normalized particle stress $\tau_{\text{part}}/\rho_f U_0^2$, both evaluated at the channel centerline and plotted against a more comprehensive set of St_K. The ratio $\tau_{\text{turb}}/\tau_{\text{turb,un}}$ in Fig. 3 (solid squares) exhibits two minima: one occurring at $\text{St}_K \approx 2$ and one occurring at $\text{St}_K \approx 30$. At the same time, the curve of $\tau_{\text{part}}/\rho_f U_0^2$ (hollow triangles) shows a single local minimum at $\text{St}_K \approx 8$. As St_K decreases towards zero, the particle stress continues to increase for reasons discussed above. As argued elsewhere [5,6], the minimum of $\tau_{\text{turb}}/\tau_{\text{turb,un}}$ at $\text{St}_K \approx 2$ and the minimum in $\tau_{\text{part}}/\rho_f U_0^2$ at $\text{St}_K \approx 8$ correspond to particle time scales which match those of near-wall vortical motions (sweeps or ejections) and large-scale Couette structures, respectively.

While Fig. 3 illustrates the strong dependence of both τ_{part} and τ_{turb} on particle Stokes number and suggests distinct St_K ranges associated with various flow structures, it only provides a partial picture in terms of the overall influence of St_K on cross-channel momentum transfer. To complete this picture, Fig. 4 plots the normalized particle stress $\tau_{\text{part}}/\rho_f U_0^2$ versus z/H for all Stokes numbers shown in Fig. 3. While the behavior shown by the hollow symbols of Fig. 3 is observed along the centerline, the peak particle stress also undergoes a strong transition with varying Stokes number: at very high or very low values of St_K, the peaks of τ_{part} located at $z/H \approx 0.1$ and 0.9 become much less pronounced and even disappear. So while particles interact with turbulent motions and exchange momentum (thus altering the magnitude of τ_{part}), another process alters the shape of the profile at the same time.

Occurring simultaneously with preferential accumulation on scales associated with these flow structures is turbophoresis, where particles collect near the walls due to wall-normal gradients in carrier phase velocity fluctuations. Figure 5 demonstrates this effect through the mass concentration profiles for the same four cases shown in Fig. 2, normalized by the homogeneous bulk concentration C_0. Figure 5 shows that very low ($\text{St}_K \approx 0.1$) and high ($\text{St}_K \approx 100$) particles maintain a more uniform concentration profile across the domain, and are subject to a lesser degree of turbophoresis than intermediate Stokes numbers. For this flow, $\text{St}_K \approx 10$ particles experience the largest concentration deficit in the channel center, followed by $\text{St}_K \approx 1$ particles. In turn, the more homogeneous concentration profiles of Fig. 5 correspond to more uniform profiles of τ_{part} across the channel in Figs. 2 and 4. Note that near-wall mass concentrations, particularly for $\text{St}_K = O(1)$ and $\text{St}_K = O(10)$, become large and may possibly violate the

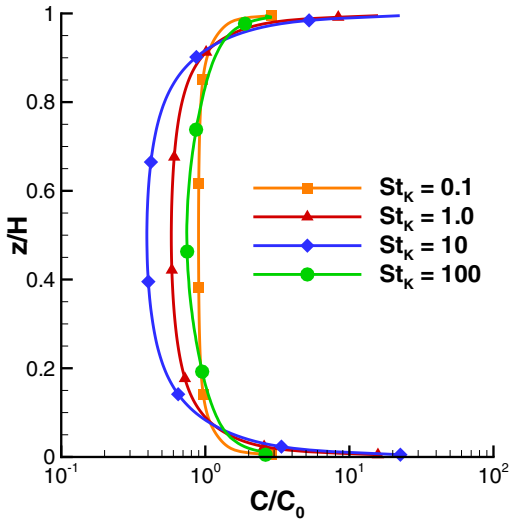

FIG. 5. Normalized mass concentration C/C_0 as a function of z/H. Cases shown are $\mathrm{St}_K \approx 0.1$ (orange); $\mathrm{St}_K \approx 1.0$ (red); $\mathrm{St}_K \approx 10$ (blue); $\mathrm{St}_K \approx 100$ (green).

assumption of negligible particle collisions, although these regions are quite small (within the viscous sublayer).

Based on Figs. 2–5 we therefore define four distinct St_K regimes: (1) $\mathrm{St}_K < 1$, where low-inertia particles increase the total stress magnitude by increasing the effective density of the fluid and where particles do not accumulate strongly; (2) $\mathrm{St}_K = O(1)$, which represents a peak in preferential concentration and a corresponding maximum reduction of turbulent stress; (3) $\mathrm{St}_K = O(10)$, where particles are too large to collect in small-scale regions near the wall but instead collect in regions associated with the Couette rollers; and (4) $\mathrm{St}_K > 50$, where particles display no strong preferential concentration or turbophoresis. It is these regimes which will form the basis of the following analysis, and as previously stated we are interested primarily in the inertial regimes 2–4.

B. Bidisperse simulations

Focusing on $\mathrm{St}_K \geqslant 1$, three simulations are performed which consist of blends of each unique combination in the set $\mathrm{St}_K \approx [1,10,100]$, where the total mass fraction $\phi_m = 0.25$ is split evenly between particles of each St_K. In addition to these three cases, monodisperse simulations at mass fractions of $\phi_m = 0.125$ (i.e., half the original) for $\mathrm{St}_K \approx [1,10,100]$ are also used to compare the total particle stress resulting from the binary blend versus adding the monodisperse particle stresses together. Figures 6(a)–6(c) show the total bidisperse particle stress (thick solid line), as well as the portion coming from each St_K (thick dashed and dotted lines), computed by evaluating $\tau_{\mathrm{part}} = \langle C \rangle \langle u_p' w_p' \rangle_c$ separately for each particle type. The total bidisperse particle stress is then compared to the individual monodisperse stresses (thin dashed and dotted lines) as well as their sum (thin solid line).

Figure 6 demonstrates that the particle stresses are nearly independent and additive, which is entirely consistent with the dilute (i.e., noninteracting) limit assumed for this study. The total particle stress of the blend nearly exactly matches the stress when summing the monodisperse simulations at half the total mass loading. This close match is best for the $\mathrm{St}_K = [10,100]$ blend [Fig. 6(c)], and worst for the $\mathrm{St}_K = [1,10]$ blend [Fig. 6(a)], particularly in the regions where τ_{part} is maximum. For cases which contain $\mathrm{St}_K \approx 1$ particles, the stress associated with these particles contributes more than half of the total, which is to be expected based on Fig. 2.

For our current purposes, the meaning of this behavior is that the particles do indeed behave nearly independently, in that particles of one St_K do not modify the flow in such a way that

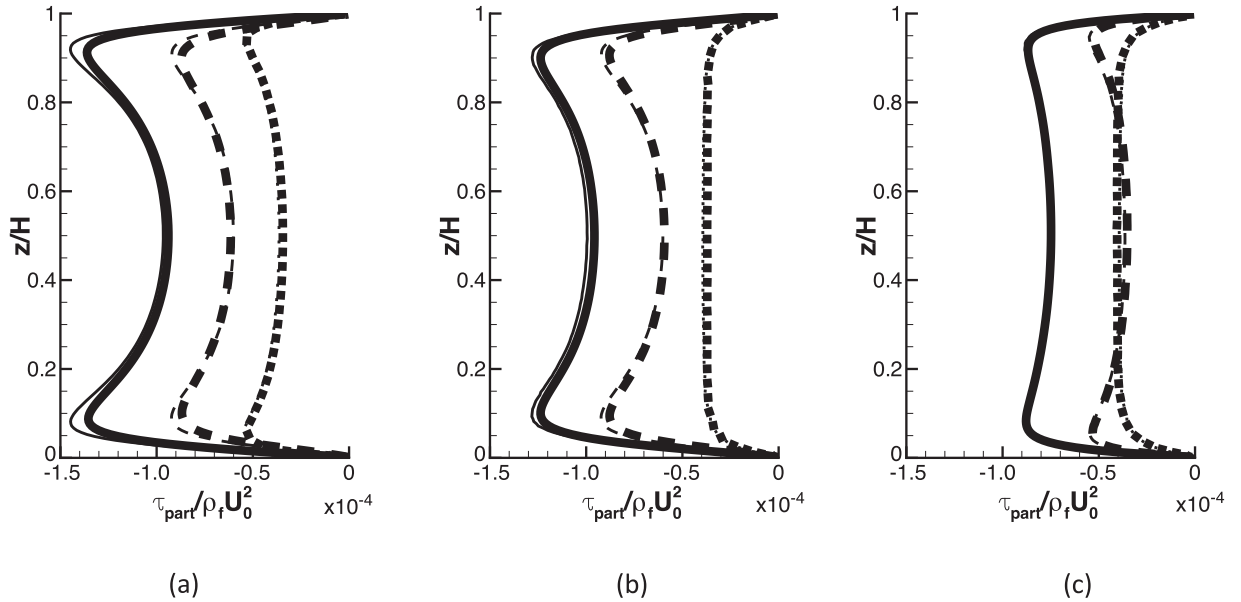

FIG. 6. Particle stress profiles $\tau_{\mathrm{part}}/\rho_f U_0^2$ (solid lines) as a function of z/H for three different bidisperse blends: (a) $\mathrm{St}_K \approx 1$ (dashed) and $\mathrm{St}_K \approx 10$ (dotted), (b) $\mathrm{St}_K \approx 1$ (dashed) and $\mathrm{St}_K \approx 100$ (dotted), and (c) $\mathrm{St}_K \approx 10$ (dashed) and $\mathrm{St}_K \approx 100$ (dotted). Thick lines denote individual and total particle stress from the bidisperse blends, thin lines denote individual and summed monodisperse particle stresses for the same St_K.

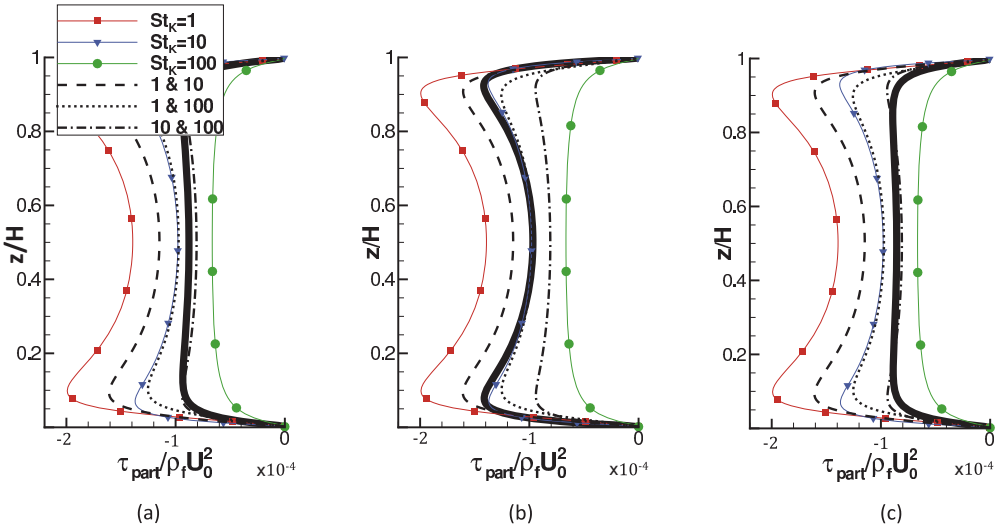

FIG. 7. Normalized particle stress $\tau_{\text{part}}/\rho_f U_0^2$ as a function of z/H for three continuous polydisperse mixtures (thick black lines): (a) $[\text{St}_{\text{min}},\text{St}_{\text{max}}] = [1,100]$; (b) $[\text{St}_{\text{min}},\text{St}_{\text{max}}] = [1,10]$; and (c) $[\text{St}_{\text{min}},\text{St}_{\text{max}}] = [10,100]$. In each figure, the particle stress from each of the original monodisperse simulations at $\text{St}_K \approx [1,10,100]$ (thin colored lines with symbols) as well as the total particle stress from each of the bidisperse simulations (thin broken black lines) are included as well—see legend in panel (a).

alters the two-way coupling of particles with a different St_K. This is consistent with the picture outlined in Sec. III A, where particles of disparate St_K interact with distinct features of the flow, e.g., $\text{St}_K = O(1)$ particles collect in and interact with near-wall streaks while $\text{St}_K = O(10)$ particles instead collect in regions associated with large-scale Couette structures. Thus a physical interpretation could be that the weakening of ejection motions due to $\text{St}_K = O(1)$ particles [6] is not expected to modify the turbulence modulation induced by larger or smaller particles, although tests (not shown here) confirm that this linearity continues to be present in bidisperse simulations even when the Stokes number is of the same order.

C. Polydisperse simulations

Based on the confirmation in Sec. III B that blends of particles with disparate St_K behave nearly independently, a final set of simulations is performed with the goal of characterizing the particle stresses which develop in continuous polydisperse mixtures at the same mass fraction of $\phi_m = 0.25$.

Each particle in the simulation is randomly chosen from a power-law distribution which is defined by a minimum and maximum St_K:

$$f(\text{St}_K) = \frac{\alpha}{\text{St}_K}, \tag{5}$$

where α is given by

$$\alpha = \frac{1}{\ln\left(\frac{\text{St}_{\text{min}}}{\text{St}_{\text{max}}}\right)}, \tag{6}$$

which is related to the mean of the distribution:

$$\overline{\text{St}}_K = \alpha(\text{St}_{\text{max}} - \text{St}_{\text{min}}). \tag{7}$$

St_{min} and St_{max} refer to the prescribed maximum and minimum St_K over which the distribution is defined, and the overbar refers to the mean of the distribution. Since the particle Stokes number is proportional to the particle mass (when the diameter is held constant, which is the case in the present simulations), the distribution given by Eq. (5) ensures that particles from each St_K contribute equally to the overall mass fraction. Thus since small St_K particles each have less mass, more of them are included to make their mass contribution equal to those of larger St_K.

Still focusing on $\text{St}_K \geqslant 1$, three continuous polydisperse mixtures are tested: (1) $[\text{St}_{\text{min}},\text{St}_{\text{max}}] = [1,100]$ where $\overline{\text{St}}_K = 22$; (2) $[\text{St}_{\text{min}},\text{St}_{\text{max}}] = [1,10]$ where $\overline{\text{St}}_K = 3.9$, and (3) $[\text{St}_{\text{min}},\text{St}_{\text{max}}] = [10,100]$ where $\overline{\text{St}}_K = 39$. For each of these continuous blends, Fig. 7 shows the particle stress τ_{part} as a function of z/H. Plotted with thin lines are the original monodisperse cases at $\text{St}_K \approx 1$, $\text{St}_K \approx 10$, and $\text{St}_K \approx 100$ and plotted with broken lines are the bidisperse cases from Sec. III B.

Figure 7 illustrates several features of the particle stress under a polydisperse loading. It is clear that particles with $\text{St}_K = O(1)$, despite having a maximum ability to reduce the turbulent stress in the monodisperse systems, do not carry a strong influence when included as part of a continuous mixture. In Fig. 7(a), where the Stokes number ranges 1–100, the magnitude of the particle stress does not approach the stress of either the monodisperse or bidisperse mixtures which contain $\text{St}_K \approx 1$ particles, indicating that their influence is overwhelmed by the presence of larger particles. Similarly in Fig. 7(b), the total mixture particle stress for a Stokes number range 1–10 is nearly equal to the particle stress for $\text{St}_K \approx 10$ particles from the monodisperse case, indicating again that $\text{St}_K = O(1)$ particles do not play a significant role in these mixtures. This is entirely consistent with Fig. 3, which shows a very rapid decrease in particle stress with Stokes number in the range $1 < \text{St}_K < 10$. Figure 7(c) shows that the mixture ranging between Stokes numbers of 10 and 100 is well represented by the binary mixture of $\text{St}_K \approx 10$ and $\text{St}_K \approx 100$.

Since the $\mathrm{St}_K = O(1)$ particles play such a small role in the overall particle stress of the polydisperse blends, and based on the fact that the bidisperse particle stress exhibited a linear behavior—i.e., the total particle stress of the binary mixture was nearly equal to the sum of the stresses of monodisperse systems at corresponding mass loadings—we compute for the $[\mathrm{St}_{\min}, \mathrm{St}_{\max}] = [1, 100]$ case an effective particle Stokes number with the goal of determining whether or not this is an adequate method of representing the entire mixture stress.

As noted above, in polydisperse systems the particle stress can be computed by

$$\tau_{\mathrm{part}} = \langle C \rangle \langle u_p' w_p' \rangle_c, \tag{8}$$

where C is the mass concentration and the average $\langle \cdot \rangle_c$ is a mass-weighted average over the dispersed phase. If instead the particles were monodisperse, a number-weighted mean could be used:

$$\tau_{\mathrm{part}} = m_p \langle n_p \rangle \langle u_p' w_p' \rangle_n, \tag{9}$$

where m_p is the particle mass (equal for all particles), n_p is the number concentration, and $\langle \cdot \rangle_n$ is the number-weighted concentration over the dispersed phase. Thus for the polydisperse case an effective particle mass $m_{p,\mathrm{eff}}$ can be computed at all heights z/H by assuming that all particles have the same mass:

$$m_{p,\mathrm{eff}} = \frac{\langle C \rangle \langle u_p' w_p' \rangle_c}{\langle n_p \rangle \langle u_p' w_p' \rangle_n}. \tag{10}$$

Figure 8 shows the profile of $\mathrm{St}_{\mathrm{eff}}$, the Stokes number corresponding to $m_{p,\mathrm{eff}}$, as a function of z/H. This is compared to both the vertical mean of this profile $\langle \mathrm{St}_{\mathrm{eff}} \rangle_z$ (dash-dotted line) as well as the mean of the distribution $\overline{\mathrm{St}}_K$ (dashed line). For modeling purposes, it would be convenient if the profile of

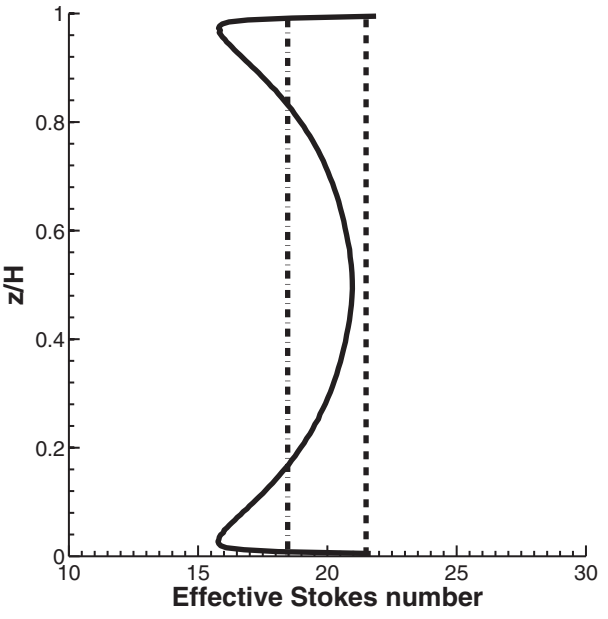

FIG. 8. Solid line: Effective Stokes number $\mathrm{St}_{\mathrm{eff}}$ computed from the effective mass of Eq. (10) for the polydisperse case $[\mathrm{St}_{\min}, \mathrm{St}_{\max}] = [1, 100]$ as a function of z/H. Dotted line: The mean of the distribution $\overline{\mathrm{St}}_K$, given by Eq. (7). Dash-dotted line: Vertical average of the $\mathrm{St}_{\mathrm{eff}}$.

$\mathrm{St}_{\mathrm{eff}}$ were uniform, which would suggest that the particle stress which develops in the system can be represented by particles of a single inertia. Figure 8 shows that indeed, the effective Stokes number deviates only within the range $15 < \mathrm{St}_{\mathrm{eff}} < 23$, which is quite narrow compared to the range of the entire mixture. It is also observed that the vertically averaged value of this profile is within roughly 5% of the mean of the distribution $\overline{\mathrm{St}}_K$, which would perhaps encourage one to merely use the distribution mean as a monodisperse value of St_K which could represent the particle stress for the whole polydisperse mixture.

To test this, Fig. 9 shows the stress components of the polydisperse case (blue) compared to the unladen case (black). Shown also are two monodisperse cases: one where the Stokes number is set to $\langle \mathrm{St}_{\mathrm{eff}} \rangle_z = 19$ (red) and one where the Stokes number is set to $\overline{\mathrm{St}}_K = 22$ (green). While all particle-laden cases show a reduction of the turbulent stress τ_{turb} nearly exactly canceled by a corresponding particle stress τ_{part} (line styles are the same as in Fig. 2), the monodisperse cases attempting to represent the polydisperse mixture overestimate the particle stress and the reduction in τ_{turb}, indicating that despite the narrow width of $\mathrm{St}_{\mathrm{eff}}$ displayed in Fig. 8, it is somewhat inadequate at representing the mixture with a single effective particle inertia. The degree of error is commensurate with the degree of variability of $\mathrm{St}_{\mathrm{eff}}$ shown in Fig. 8.

The failure of representing the mixture with a single particle is perhaps unsurprising given the complex relationship between τ_{part} and St_K, but based on the discussion surrounding Figs. 3–5, we suggest that to represent the particle stress in the polydisperse system, one must at a minimum represent particles from each of the four Stokes number regimes outlined previously. That is, given the varying importance of turbophoresis and preferential accumulation across different St_K, a single particle type will not be sufficient to act effectively as a mixture even given the results of Fig. 8. If a mixture contains some particles which can collect at the walls (e.g., $\mathrm{St}_K \approx 10$) in addition to others that remain evenly distributed throughout the domain (e.g., $\mathrm{St}_K \approx 100$), these two distinct behaviors must be represented in any attempt to model the blend.

To this end, we perform one final simulation where, based on Figs. 3–5 and the previous outline of distinct St_K regimes, we define the following Stokes number ranges along with a single St_K to represent each range: $1 < \mathrm{St}_K < 2$ represented by $\mathrm{St}_K = 1$; $2 < \mathrm{St}_K < 50$ represented by $\mathrm{St}_K = 10$; and $\mathrm{St} > 50$ represented by $\mathrm{St}_K = 100$. Then, based on the mixture $[\mathrm{St}_{\min}, \mathrm{St}_{\max}] = [1, 100]$ currently under discussion, the mass fraction included from each of these ranges is chosen proportionally based on its fraction of the range $1 < \mathrm{St}_K < 100$. For this specific case, this leads to 1% of the total mass fraction represented by $\mathrm{St}_K = 1$ particles, 48.5% represented by $\mathrm{St}_K = 10$ particles, and 50.5% represented by $\mathrm{St}_K = 100$ particles. It is interesting to note that despite its small percentage contribution in this model, the effect of the $\mathrm{St}_K = 1$ particles, due to their optimal turbulent flux modification (cf. Fig. 3), is relatively small yet not insignificant compared to $\mathrm{St}_K = 10$ and $\mathrm{St}_K = 100$ particles when considering the wide range of St_K in this particular mixture.

The stress components for this test model are included in Fig. 9 as orange lines, and are seen to very closely approximate

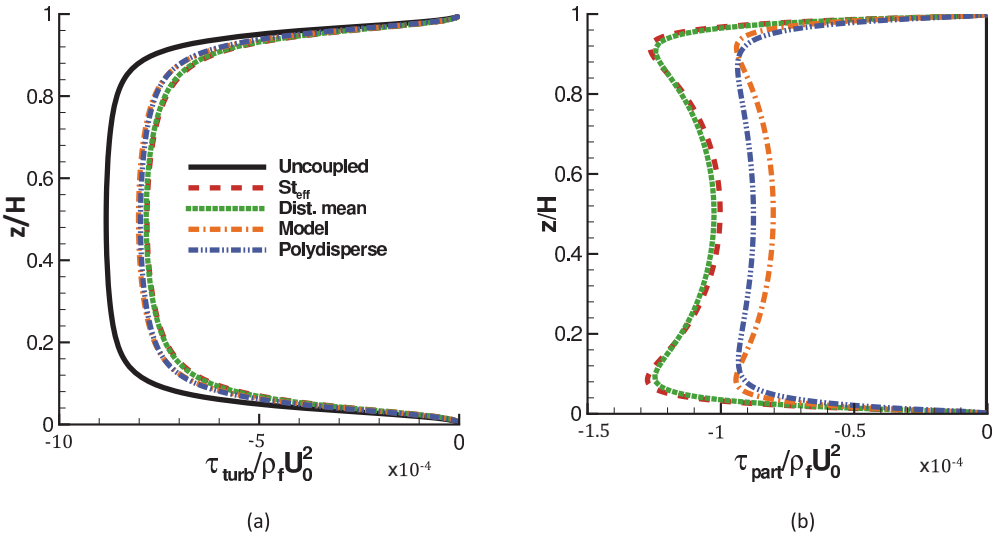

FIG. 9. (a) Turbulent stress τ_{turb} and (b) particle stress τ_{part} as a function of height for the polydisperse case $[\text{St}_{\text{min}},\text{St}_{\text{max}}] = [1,100]$, where the color and line style is given in the legend: the full polydisperse mixture (blue, dash-dot-dot); a monodisperse system with the Stokes number set to the distribution mean $\overline{\text{St}}_K$ (green, dotted); a monodisperse system with the Stokes number set to the vertically averaged effective Stokes number $\langle \text{St}_{\text{eff}} \rangle_z$ (red, dashed); and a model case with representation from each of the Stokes number regimes (orange, dash-dot). Also shown for comparison is the unladen case (black, solid). All stress components normalized by $\rho_f U_0^2$.

the polydisperse stress components. While not shown here for brevity, the same is true for the other polydisperse cases considered in Fig. 7. We thus conclude that, as a minimum, each of the distinct Stokes number regimes outlined in Sec. III A must be represented in an attempt to mimic the particle stresses which develop in the polydisperse case. Admittedly, the specific boundaries of these regimes were chosen somewhat arbitrarily, but reflect the Stokes number sensitivity represented in Fig. 3. For instance the range represented by $\text{St}_K \approx 1$ particles is quite narrow, while the behavior associated with $\text{St}_K \approx 10$ particles is quite broad.

IV. CONCLUSIONS

In this study we have performed simulations of two-way coupled turbulent planar Couette flow, with the intent of understanding and representing the momentum carried by polydisperse particle mixtures at friction Reynolds numbers of $\text{Re}_\tau \approx 120$. The study is broken up into three sequential segments, each with its own specific findings:

(1) First, monodisperse simulations were carried out in the range $0.1 < \text{St}_K < 100$ and the changes in the particle stress τ_{part} were used to define four Stokes number regimes: (i) $\text{St}_K < 1$, where low-inertia particles only weakly preferentially accumulate and whose particle stress effectively adds to the density of the carrier phase; (ii) $\text{St}_K = O(1)$, where particles can efficiently preferentially concentrate and in this way result in a maximum reduction of the carrier phase turbulent stress; (iii) $2 \lesssim \text{St}_K \lesssim 50$, where particles accumulate in regions associated with the large-scale Couette structures in addition to turbophoresis; and (iv) $\text{St}_K \gtrsim 50$, where particles are too inertial to exhibit preferential concentration or turbophoresis.

(2) Systems of bidisperse blends of particles taken by each combination in the set $\text{St}_K \approx [1,10,100]$, where half of the total dispersed phase mass fraction is represented by each St_K, were used to demonstrate the nearly additive property of the particle stress. The total stress in bidisperse systems is nearly exactly equal to the sum of the monodisperse cases at the corresponding mass fraction and Stokes numbers.

(3) Polydisperse blends of particles, where each particle St_K is drawn from a power-law distribution defined over a prescribed Stokes number range, were computed. It was shown that a single effective particle Stokes number is not necessarily sufficient for representing the particle stress and corresponding reduction in turbulent stress, and that mass-proportional representation from each of the Stokes number regimes identified with the monodisperse computations provides an accurate model for the continuously polydisperse blend.

The present simulations are meant to demonstrate ways in which dilute systems of polydisperse particles, which occur very frequently in natural and industrial environments, can be represented by a simplified description of the dispersed phase. In this sense it is the ultimate goal of our ongoing work to use these findings in order to develop effective models which minimize the need for explicitly representing all particle sizes in a polydisperse mixture. A first attempt at such a model could include parametrizing the particle stress as a function of Stokes number (i.e., particle size) and integrating over all particles available in a given mixture, however as shown by the significant height dependence in Fig. 4, such a technique would be specific to the idealized geometry used here and would be thus limited in its universality. It is likely that models would instead need to be built based on more general mechanistic findings revealed by this study: for instance the presence of $\text{St}_K \ll 1$ particles may possibly be modeled solely through a modified fluid density while $\text{St}_K \gg 1$ particles can be modeled from a stochastic point of view (see, e.g., Février *et al.* [13]), leaving only particles which preferentially accumulate to be explicitly represented in a simulation. Finally the addition of particle-particle collisions in less dilute systems

will likely significantly modify the present findings, since particles with disparate St_K can directly interact (as opposed to only interacting indirectly through modifications to the surrounding flow), and remains an interesting point of continuing research.

ACKNOWLEDGMENT

The authors would like to thank the Computing Research Center at the University of Notre Dame for computational support and access to local resources.

[1] S. Balachandar and J. K. Eaton, Annu. Rev. Fluid Mech. **42**, 111 (2010).
[2] G. Sardina, P. Schlatter, L. Brandt, F. Picano, and C. M. Casciola, J. Fluid Mech. **699**, 50 (2012).
[3] D. W. I. Rouson and J. K. Eaton, J. Fluid Mech. **428**, 149 (2001).
[4] E. Russo, J. G. M. Kuerten, C. W. M. van der Geld, and B. J. Geurts, J. Fluid Mech. **749**, 666 (2014).
[5] D. H. Richter and P. P. Sullivan, Phys. Fluids **25**, 053304 (2013).
[6] D. H. Richter and P. P. Sullivan, Phys. Fluids **26**, 103304 (2014).
[7] D. H. Richter, Phys. Fluids **27**, 063304 (2015).
[8] J. Borée and N. Caraman, Phys. Fluids **17**, 055108 (2005).
[9] M. R. Maxey and J. J. Riley, Phys. Fluids **26**, 883 (1983).
[10] R. Clift, J. R. Grace, and M. E. Weber, *Bubbles, Drops, and Particles* (Academic, Berkeley, CA, 1978).
[11] T. Tsukahara, H. Kawamura, and K. Shingai, J. Turbul. **7**, N19 (2006).
[12] J. Lee and C. Lee, Phys. Fluids **27**, 023303 (2015).
[13] P. Février, O. Simonin, and K. D. Squires, J. Fluid Mech. **533**, 1 (2005).